Rayleigh-Bénard turbulence modified by two-way coupled inertial, nonisothermal particles

Hyungwon John Park*
Department of Aerospace and Mechanical Engineering, University of Notre Dame, Notre Dame, Indiana 46556, USA

Kevin O'Keefe and David H. Richter
Department of Civil and Environmental Engineering and Earth Sciences, University of Notre Dame, Notre Dame, Indiana 46556, USA

(Received 16 August 2017; published 22 March 2018)

Direct numerical simulation (DNS) combined with the Lagrangian point particle model is used to study Rayleigh-Bénard convection in order to understand modifications due to the interaction of inertial, nonisothermal particles with buoyancy-driven turbulence. In this system, turbulence can be altered through direct momentum coupling, as well as through buoyancy modification via thermal coupling between phases. We quantify the effect of the dispersed phase by changes to the total integrated turbulent kinetic energy (TKE) and Nusselt number (Nu). The dispersed particles experience gravitational settling and are introduced at the lower wall so that turbulence must overcome the settling velocity for the particles to vertically distribute throughout the domain. We focus primarily on particle inertia, settling velocity, mass fraction, and the ratio of the particle to fluid specific heat. Furthermore, individual contributions by the momentum coupling and thermal coupling are studied to see which most significantly changes Nu and TKE. Our results show that particles with Stokes number of order unity maximize Nu, corresponding to a peak of clustering and attenuation of TKE. Increased mass fractions lead to a linear increase of Nu and decrease of TKE. With varying specific heat ratio, Nu and TKE exhibit monotonic behaviors, where in the high limit particles become isothermal and depend upon the initialized particle temperature. It is also shown that particles two-way coupled only through momentum attenuate Nu and weaken TKE, while thermal-only coupling also weakens TKE but enhances Nu. When both couplings are present, however, thermal coupling overwhelms the momentum coupling attenuation, and the net result is an enhancement of Nu.

DOI: 10.1103/PhysRevFluids.3.034307

I. INTRODUCTION

In a wide variety of natural and industrial systems, turbulent flows suspend particulate matter which, depending on circumstances, can influence the flow and modify the overall transport of heat, momentum, and mass. This two-way coupling phenomenon has been studied extensively in various wall-bounded and homogeneous turbulent flow simulations [1–7], where the influences of particle inertia, concentration, and/or settling velocity on a multitude of statistical and dynamical characteristics of the turbulence have been examined in detail. Relatively speaking, however, numerical studies on the effects of nonisothermal particles are much fewer in number and primarily focus on the ability of heat-conducting particles to modify heat transfer or alter temperature

*Hpark6@nd.edu

fluctuation statistics of the carrier fluid [8–11]. Even fewer are investigations which consider the multiple feedback effects of the particles on the turbulent kinetic energy of the fluid—via both direct momentum exchange as well as thermal feedback through buoyancy forces.

In wall-bounded turbulent flows, it has been repeatedly demonstrated that small, two-way coupled particles can directly weaken near-wall coherent structures, particularly when the response time of the particle is near that of the coherent motions [5,12]. At the same time, these small particles can have a more complex influence on turbulent kinetic energy since the suppression of these coherent structures can strengthen near-wall streaks, thereby enhancing velocity variance near the walls [13–15]. In the presence of thermally coupled particles and buoyancy-driven turbulence, however, these (and other) influences of momentum coupling between the carrier and particle phases will be combined with the thermally induced changes to the turbulent flow, since in many cases thermally coupled particles are found to enhance temperature fluctuations and modify mean temperature gradients of the fluid [10,11].

Recently, Frankel *et al.* [16] demonstrated that particles heated externally via irradiation in homogeneous turbulence can significantly modify turbulent kinetic energy (TKE) and mean particle settling velocities via buoyant plumes emerging from hot, clustered particles. While in this case the particle temperatures were quite high, buoyant updrafts were created that could exceed the settling velocity of the particles, and the resulting turbulent kinetic energy of the carrier fluid can be enhanced due to increased buoyancy production. Characteristics of this particle- or buoyancy-induced turbulence is described by Zamansky *et al.* [17,18], where turbulence in otherwise quiescent fields is created by heating particles and establishes a feedback loop where turbulence causes particle clustering, which concentrates the particle heat sources, thereby causing further turbulence production.

In the present study our aim is to further explore the role of thermally and dynamically coupled particles in buoyancy-driven turbulent flow, but in systems where the particles are not externally heated. We use turbulent Rayleigh-Bénard (RB) flow as an idealized test configuration and focus on the relative balance between dynamic and thermal coupling between the particles and surrounding fluid. In this context, several studies have examined the role of small bubbles in RB flow. It has been observed that vapor bubbles in liquid can contribute in multiple ways to the surrounding flow: their radial change indicates a sensible and latent heat exchange with the surrounding fluid and therefore a carrying capacity for heat across the domain, and their buoyancy can strengthen the cellular up- and downdrafts commonly observed in RB convection [19,20]. In many cases the overall Nusselt number is enhanced, although the bubbles can damp out temperature gradients which give rise to increased buoyant production of TKE. The enhanced Nusselt number is seen over a wide range of flow Rayleigh numbers, and the bubbles are particularly effective when they have large potential for growth [21].

While the effects of bubbles and boiling have far-reaching implications on heat transfer in buoyancy-driven systems, we are instead focused, in this study, on the effects of solid particles in gas-phase turbulence, particularly when the particles must be lifted by the turbulence from the lower boundary into the interior of the domain. In a somewhat similar setup, Oresta and Prosperetti [22] performed simulations of RB flow where solid particles were allowed to settle from the top boundary downwards, and whose temperature was specified (i.e., the particles were isothermal). Simulations were performed over a wide range of particle diameters, and it was found that mechanical and thermal coupling can both substantially change the overall heat transfer, mean particle settling velocities, and flow patterns in the system. We intend to further this understanding by investigating particles whose temperature is nonisothermal, and whose suspension is dictated by the turbulence which it can modify through both mechanical and thermal coupling.

II. METHOD

Our goal is to investigate the influence of thermally conducting particles which are smaller than the smallest scales of the turbulence, so we therefore invoke the point particle assumption and track

individual particles as Lagrangian points with their own mass and temperature. At the same time, the continuous carrier phase is solved via direct numerical simulation (DNS) on an Eulerian grid and is subject to the Navier-Stokes equations under the Boussinesq approximation:

$$\frac{\partial u_i}{\partial x_i} = 0, \tag{1}$$

$$\rho_f \frac{Du_i}{Dt} = -\frac{\partial p}{\partial x_i} + \mu_f \frac{\partial^2 u_i}{\partial x_j^2} + \beta T' g \rho_f \delta_{3i} + F_i, \tag{2}$$

$$\rho_f C_{p,f} \frac{DT}{Dt} = k_f \frac{\partial^2 T}{\partial x_j^2} + S, \tag{3}$$

where u_i is the fluid velocity, ρ_f is the fluid density, p is the pressure, μ_f is the fluid dynamic viscosity, $C_{p,f}$ is the specific heat of the fluid, k_f is the thermal conductivity of the fluid, g is the acceleration of gravity, δ is the Kronecker delta, and $\beta = 1/T_0$ is the thermal expansion coefficient (assuming the Boussinesq limit and an ideal gas, where T_0 is the reference temperature). The temperature deviation $T' = T - T_0$ is the deviation of the temperature from the reference state (taken herein as the cold plate temperature). The terms F_i and S represent the momentum and thermal two-way coupling between the carrier and dispersed phases, and are computed by summing the net momentum and energy gained or lost by the particles and distributing to the surrounding grid points.

Likewise, mass, momentum, and energy conservation of the dispersed phase yield the following equations for each individual particle:

$$\frac{dx_i}{dt} = v_i, \tag{4}$$

$$\frac{dv_i}{dt} = \frac{1}{\tau_p}(u_{f,i} - v_i) + g\delta_{3i}, \tag{5}$$

$$\frac{dT_p}{dt} = \frac{(T_f - T_p)}{\tau_T}, \tag{6}$$

where terms other than gravity and hydrodynamic drag have been neglected from the particle momentum equation since the density ratio between the carrier and particle phase is large, and Stokes drag is assumed because the particle Reynolds numbers remain small [23]. The particle position x_i evolves according to its velocity v_i, and T_p is the particle temperature. The fluid velocity $u_{f,i}$ and temperature T_f at the particle location are interpolated using sixth-order Lagrange interpolation. In Eq. (5), $\tau_p = (\rho_p d_p^2)/(18\mu_f)$ is the Stokes acceleration time scale of the particle, where d_p is the particle diameter and ρ_p is the particle density. In Eq. (6), $\tau_T = (3\tau_p \mathrm{Pr} C_{p,p})/(C_{p,f}\mathrm{Nu}_p)$ is the thermal time scale of the particle, where $C_{p,p}$ is the particle-specific heat and $\mathrm{Pr} = \nu_f/\alpha_f$ is the fluid Prandtl number, where $\nu_f = \mu_f/\rho_f$ is the fluid kinematic viscosity and $\alpha_f = k_f/(\rho_f C_{p,f})$ is the fluid thermal diffusivity. For flow past a spherical droplet, Nu_p is obtained from a dimensionless empirical correlation [24]:

$$\mathrm{Nu}_p = 2 + 0.6\mathrm{Re}_p^{1/2}\mathrm{Pr}^{1/3}, \tag{7}$$

where $\mathrm{Re}_p = |v_i - u_{f,i}|\rho_f d_p/\mu_f$ is the particle Reynolds number. The notation $|v_i - u_{f,i}|$ refers to the magnitude of the vector difference between the fluid and particle velocities.

Equations (1)–(6) are solved using the same numerical code as used previously in our research group [7,25–27], so only a brief summary is provided here. The code is periodic in the horizontal x and y directions and uses a stretched grid in the vertical z direction. A pseudospectral discretization is used in the horizontal directions, and second-order finite differences are used in the vertical direction. Time integration for both the particle and carrier phases is done with a third-order Runge-Kutta scheme, and the divergence-free velocity field of the carrier phase is enforced via a fractional step method.

TABLE I. Baseline fluid and particle properties. These parameters are constant unless specifically varied in subsequent sections.

Parameter	Value
Ra	2×10^6
H	0.116 m
L_x, L_y	0.348 m
U_{buoy}	0.204 m s^{-1}
ρ_f	1.29 kg m^{-3}
ν_f	1.37×10^{-5} m^2 s^{-1}
α_f	2.02×10^{-5} m^2 s^{-1}
Pr	0.678
ΔT	10.0 °C
ϕ_m	0.05
$C_{p,f}$	1.0 kJ kg^{-1} K^{-1}
$C_{p,p}$	4.179 kJ kg^{-1} K^{-1}

The numerical domain is rectangular with a size of $3H \times 3H \times H$ and a grid of $[N_x, N_y, N_z] = [128, 128, 128]$. A stretched, nonuniform grid is used in the z direction to resolve the boundary layers. Boundary conditions for the carrier phase are of the Dirichlet type at the upper and lower boundaries: no-slip for all three velocity components and specified temperatures $T_{\text{top}} = 300.15$ K and $T_{\text{bot}} = 310.15$ K at the upper and lower boundaries, respectively. For the particles, an elastic reflection is enforced at the upper boundary (equivalent to a no-flux condition), and the particle is removed when crossing the lower boundary.

In this study we are particularly interested in systems where the dispersed phase must be suspended by the turbulence from below, akin to physical processes such as aeolian saltation [28]. Therefore for each particle which is removed at the lower boundary due to gravitational settling, we reinsert a particle which possesses the same velocity and temperature as the exiting particle, and place it at a randomly chosen location in the lower 10% of the domain. By giving the new particle the same properties as the exiting particle, we ensure that the particle phase does not represent an external source of heat or momentum, unlike previous studies [22]. The maximum reinsertion height of $z/H = 0.1$ is based on the crossover point between diffusive and turbulent momentum fluxes; at this point turbulent transport of heat and momentum begins to dominate over diffusive transport, and we take this as a location where turbulence can potentially lift particles into the interior of the domain. The reinjection percentage (the average number of particles reinjected per time step, normalized by the total number of particles) is around 0.2% for St ≈ 10.0 and much smaller (0.002%) for St ≈ 0.1 for low settling velocities. This percentage increases with settling velocity at all St.

For all numerical simulations herein, the Rayleigh number of the flow, $\text{Ra} = (g\beta\Delta T H^3)/(\nu_f \alpha_f)$, is set to 2×10^6, where $\Delta T = T_{\text{bot}} - T_{\text{top}}$ is the difference in plate temperature. In all cases, the particle temperature is initialized at $T_{p,\text{init}} = 305$ K. Other constant properties of the simulations are shown in Table I. Unladen simulations were validated against experimental Nu-Ra relationships [29], while Nu from isothermal, particle-laden simulations were compared to previous numerical results [22] (Nu defined below). The centerline Taylor-scale Reynolds number Re_λ is approximately 50. Particle-laden simulations are initialized by placing particles at random locations within a previously obtained unladen turbulent field. We perform a series of simulations to investigate four key dimensionless parameters which govern this multiphase system:

(1) The particle inertia, as described by the Stokes number $\text{St} = \tau_p/\tau_f$, where τ_p was defined above and where τ_f is chosen here as the Kolmogorov fluid time scale $\tau_f = (\nu/\overline{\epsilon})^{1/2}$, where $\overline{\epsilon}$ is the vertically averaged rate of dissipation of turbulence kinetic energy. The local Kolmogorov time scale does not vary significantly from the effects of the two-way coupled system, and the vertical profile of ϵ does not deviate significantly from the vertically averaged value [see Fig. 8(a)].

(2) The dimensionless particle settling velocity V_g/U_{buoy}, where $V_g = \tau_p g$ is the particle terminal velocity and $U_{\text{buoy}} = \sqrt{g\beta\Delta T H}$ is a buoyancy velocity scale.

(3) The particle mass fraction ϕ_m, which is defined as the total mass of particles in the system to mass of carrier phase.

(4) The specific heat ratio $C_{p,p}/C_{p,f}$.

We also vary the couplings (i.e., thermal and dynamic) to determine which leads to a larger influence on the carrier phase heat transfer and turbulence. In the next section, the findings from each of these simulation sets will be described in detail.

III. RESULTS

A. Particle inertia and settling velocity

It is well known that particle inertia leads to preferential clustering [30], and that the combination of inertial clustering and gravitational settling can lead to preferential sweeping and enhanced vertical velocities [31,32]. Therefore in light of this interplay between inertia and gravity, we begin by discussing results from a series of simulations which vary St and V_g/U_{buoy} independently, in order to understand the relative roles of inertia and settling on modulation of turbulence in the system. Numerous simulations were run across the two-dimensional parameter space ranging between $10^{-1} < \text{St} < 15$ and $10^{-4} < V_g/U_{\text{buoy}} < 0.1$. In all cases, once the simulations reaches $t^* \approx 175$, where $t^* = tU_{\text{buoy}}/H$, a statistically steady state is achieved. From this point, time averaging is performed until $t^* \approx 1400$, leading to average quantities (such as vertical particle concentration and temperature distribution) statistically converged within 1%.

Figure 1 qualitatively demonstrates the effect of particle inertia on clustering by providing instantaneous snapshots of normalized fluid temperature (color contours) and particle location (black dots) for varying St at constant $V_g/U_{\text{buoy}} = 10^{-3}$. From the figure it is apparent that particles with $\text{St} \approx 1$ tend to cluster into bands which are closely aligned with the up- and downdrafts of the RB convection cells, while for much larger and smaller St, the particles remain more homogeneously distributed throughout the domain. Note that the number of particles is different since the mass concentration is held constant at $\phi_m = 0.05$ (ϕ_m is the ratio of particle mass to fluid mass in the system).

As with shear-driven turbulent flows, particles drift toward the walls in the absence of gravitational settling due to turbophoresis [33,34], despite significant differences in near-wall coherent structures

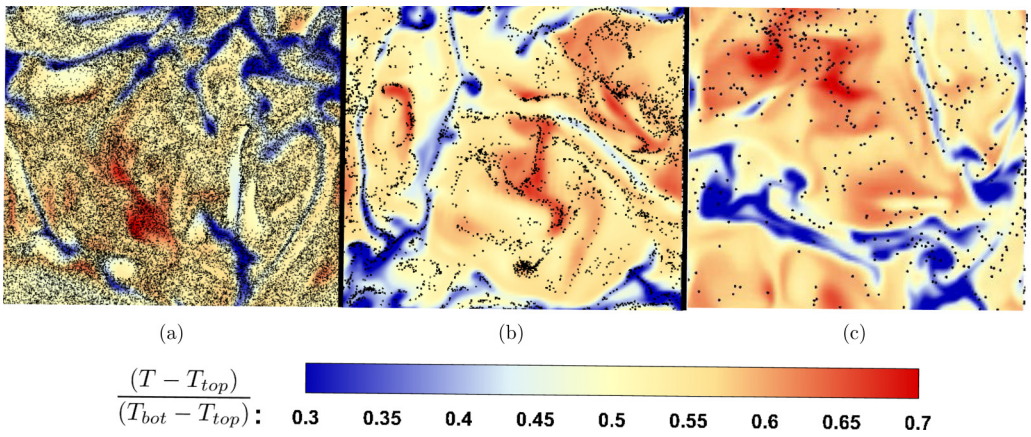

FIG. 1. Instantaneous snapshots of normalized temperature contours in a top-down view at a height of $z/H = 0.8$ for (a) $\text{St} \approx 0.1$, (b) $\text{St} \approx 1$, and (c) $\text{St} \approx 10$. Black dots represent particles, and the slice is taken at a height of $z/H = 0.85$. $V_g/U_{\text{buoy}} = 10^{-3}$ for these cases.

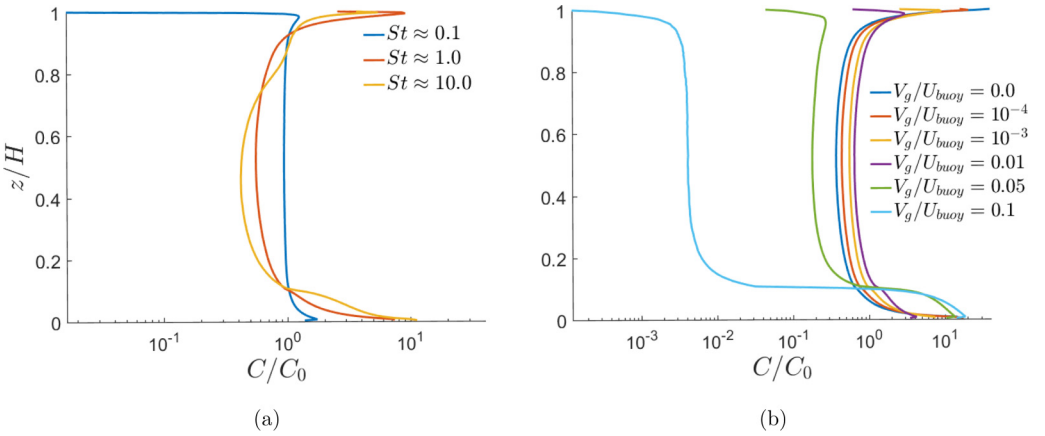

FIG. 2. Profiles of normalized number concentration for (a) varying St at a constant $V_g/U_{\text{buoy}} = 10^{-3}$ and (b) varying V_g/U_{buoy} at a constant St ≈ 1.

between turbulent channel and RB flows. Figure 2(a) shows that this effect is of similar magnitude at both St ≈ 1 and St ≈ 10, and that for St ≈ 0.1 the particles are more or less distributed evenly across the vertical direction since they behave mostly as fluid tracers (except at the walls, where boundary conditions cause deviations). The relatively small settling velocity in Fig. 2(a), $V_g/U_{\text{buoy}} = 10^{-3}$, induces a small measure of asymmetry in all three profiles, but this settling is not large enough to overcome the drift toward both walls.

At a constant Stokes number of St ≈ 1, the effect of increasing the settling velocity is shown in Fig. 2(b). Here small increases of settling velocity actually increase the concentrations near the center line ($z/H = 0.5$), as the downward settling begins to overcome upward turbophoretic drift. Eventually, at strengths around $V_g/U_{\text{buoy}} = 0.05$, the gravitational settling becomes too strong for the flow to maintain suspension, and by $V_g/U_{\text{buoy}} = 0.1$ the particles are nearly all settled at the bottom. For these largest settling velocities, there is a sharp discontinuity in concentration at $z/H = 0.1$ due to the random injection location of regenerated particles in the bottom 10% of the domain.

As a basis for understanding and explaining modifications to turbulence and heat transfer due to the two-way coupling of the particles, Fig. 3 presents several quantities associated with the particles' ability to thermally interact with the flow, as a function of St at a constant $V_g/U_{\text{buoy}} = 10^{-3}$.

First, Figs. 3(a) and 3(b) show that the overall mean temperature in the system is only slightly modified as a result of the two-way coupled particles, but the particle temperature can deviate substantially from the local fluid temperature. For $C_{p,p}/C_{p,f} = 4.179$, the thermal time scale τ_T is about four times that of the Stokes acceleration time scale τ_p (see, for example, Nakhaei and Lessani [11] or Zonta *et al.* [8]). This, in effect, leads to a thermal Stokes number (defined as $\text{St}_T = \tau_T/\tau_f$) to be four times that of the momentum-based St. As the Stokes number increases, the overall magnitude of the difference between the fluid and particle temperatures increases due to the particles' higher thermal inertia. The reinjection procedure of setting the new particle temperature equal to the departing particle temperature causes a small kink at $z/H = 0.1$ for high particle inertia, which again results because higher St particles cannot adjust their temperature as quickly as low St particles.

This inability of particles to quickly adjust to the local fluid temperature is what drives the thermal coupling between the dispersed phase and the fluid, which in turn modifies heat transfer and turbulence in the RB system (more will be said on this below). To further quantify this thermal disequilibrium, Fig. 3(c) shows mean profiles of the difference between the particle temperature and the fluid temperature seen by the particles. It is this quantity which appears in the right-hand side of Eq. (6), driving heat exchange between the particle and fluid. In the study of Oresta and Prosperetti [22], the particle temperature was assumed constant, so this quantity only reflected fluid temperatures

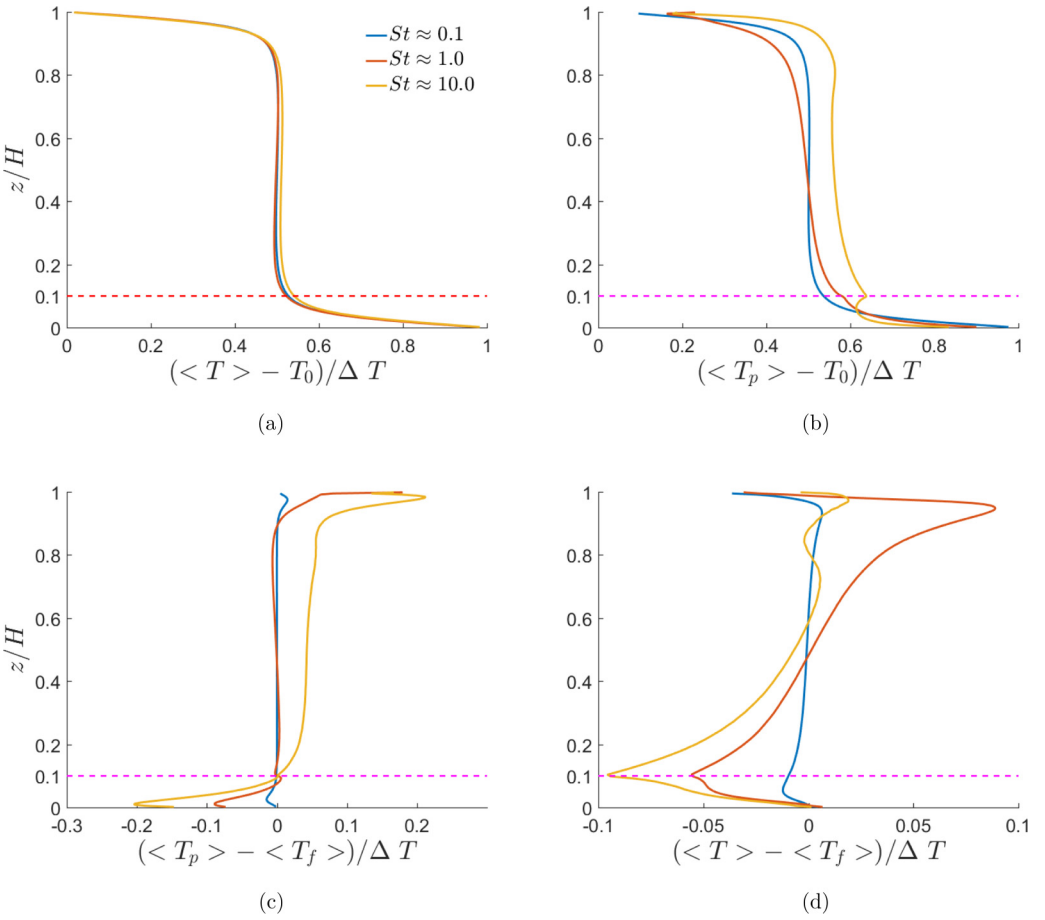

FIG. 3. Normalized, mean vertical profiles of (a) fluid temperature $\langle T \rangle$, (b) particle temperature $\langle T_p \rangle$, (c) difference between average particle temperature and average fluid temperature seen by the particles $\langle T_p \rangle - \langle T_f \rangle$, and (d) difference between fluid temperature and fluid temperature seen by the particles $\langle T \rangle - \langle T_f \rangle$. The dashed horizontal reference line represents the maximum reinjection height of $z/H = 0.1$. Shown are three different Stokes numbers at a constant $V_g/U_{\text{buoy}} = 10^{-3}$.

seen by the particle and would not be as sensitive to the Stokes number. Here Fig. 3(c) shows that with increasing Stokes number, the overall degree of disequilibrium between the particle temperature and the local fluid temperature increases, which again is consistent with the higher thermal inertia of the larger St particles. A similar feature is seen in Nakhaei and Lessani [11]. Above the reinjection height of $z/H = 0.1$, particles are almost all warmer than their surroundings, while below $z/H = 0.1$ the particles are always cooler due to their removal and replacement as they settle out of the bottom domain.

Finally, Fig. 3(d) shows a slightly different quantity: the difference between horizontally averaged fluid temperature and the average temperature seen by the particles. In the case of particles which are homogeneously distributed across the horizontal plane, this difference would be zero since the particles would uniformly sample all of the fluid temperatures in the plane. Therefore, the difference $\langle T \rangle - \langle T_f \rangle$ indicates particles preferentially collecting in regions where the temperature does not equal the true horizontal mean. Indeed, Fig. 3(d) shows that particles of St ≈ 0.1 show very small differences between these temperatures, which is consistent with the qualitative observation of Fig. 1(a). In the upper portion of the domain, this difference is maximum and positive for St ≈ 1, indicating that particles are preferentially residing in areas where the local temperature is cooler than

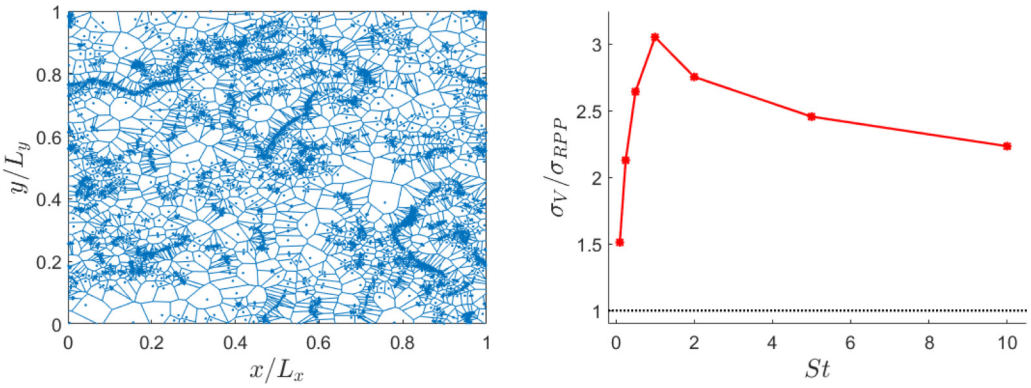

(a) (b)

FIG. 4. (a) Instantaneous Voronoï diagram for St ≈ 1 taken at $z/H = 0.5$ for a slice of thickness 2η (the Kolmogorov length scale) with $V_g/U_{\text{buoy}} = 10^{-3}$. (b) Standard deviation of the normalized Voronoï area σ_V, normalized by that of a random Poisson process, σ_{RPP}, as a function of St.

the horizontal average (i.e., downdrafts). Near the bottom, the particles reside in regions warmer than the mean (i.e., updrafts), and this effect is modified by the lower boundary condition.

An alternative way to identify particle clustering can be done through Voronoï diagrams [35]. Here Voronoï cells are drawn, and their areas are inversely related to the local concentrations; their statistical distribution can be used to quantify clustering. In Fig. 4(a) the Voronoï cell areas are visualized for a representative slice taken at $z/H = 0.5$ for the St ≈ 1, $V_g/U_{\text{buoy}} = 10^{-3}$ case. We then compare the statistical distribution of Voronoï areas to that of a random Poisson process and compare the standard deviation σ_V to identify clustering.

Figure 4(b) presents the ratio σ_V/σ_{RPP} as a function of St for $V_g/U_{\text{buoy}} = 10^{-3}$, where σ_{RPP} is the standard deviation of Voronoï areas if particles were randomly distributed. The figure shows the greatest clustering for St at order unity. In the limits of low and high St, σ_V approaches σ_{RPP} as particles become tracers on the low end, and as particles become unresponsive to velocity fluctuations on the high end.

In this study we focus on two intertwined effects of the particles: altering the cross-channel heat transfer, and modifying the characteristics of the turbulence. The former is quantified by the channel Nusselt number: $\text{Nu} = \overline{q}H/(k_f \Delta T)$, where $\overline{q}$ is the total heat flux from the bottom to the top boundary. We measure the latter by the vertically integrated turbulent kinetic energy, $\text{TKE} = \frac{1}{H}\int_0^H k\, dz$, where $k(z) = \frac{1}{2}\langle u'^2 + v'^2 + w'^2\rangle$ is the mean TKE at each height.

Figure 5 presents a cross section of our results holding St ≈ 1 constant while varying the settling velocity, in order to observe changes to heat transfer and turbulence. From Fig. 5(a), the addition of nonisothermal, two-way coupled particles leads to an increased Nu compared to the unladen case, regardless of settling velocity. In the limit of vanishing gravitational settling, Nu approaches a gravity-free limit of roughly 15% higher than the unladen value, while in the limit of high settling velocity, Nu approaches the unladen value as all of the particles are confined to the lowest 10% of the domain. Between these limits, peaking around $V_g/U_{\text{buoy}} \approx 10^{-3}$, the enhancement of Nu reaches a maximum, which we argue is linked to the increased concentration in the domain center as gravitational settling overcomes upwards turbophoretic drift [cf. Fig. 2(b)].

Figure 5(b), on the other hand, shows that the turbulence of the system is actually weakened compared to the unladen case for nearly all settling velocities. Again, the limit of low V_g/U_{buoy} approaches the gravity-free damping of TKE, while the upper limit approaches a value near the unladen case, and the peak damping of TKE occurs now closer to $V_g/U_{\text{buoy}} \approx 10^{-2}$.

For understanding the effects of particle inertia, Fig. 6 shows the converse of Fig. 5: the settling velocity is held constant at $V_g/U_{\text{buoy}} = 10^{-3}$ while St is varied between $0.1 < \text{St} < 15$.

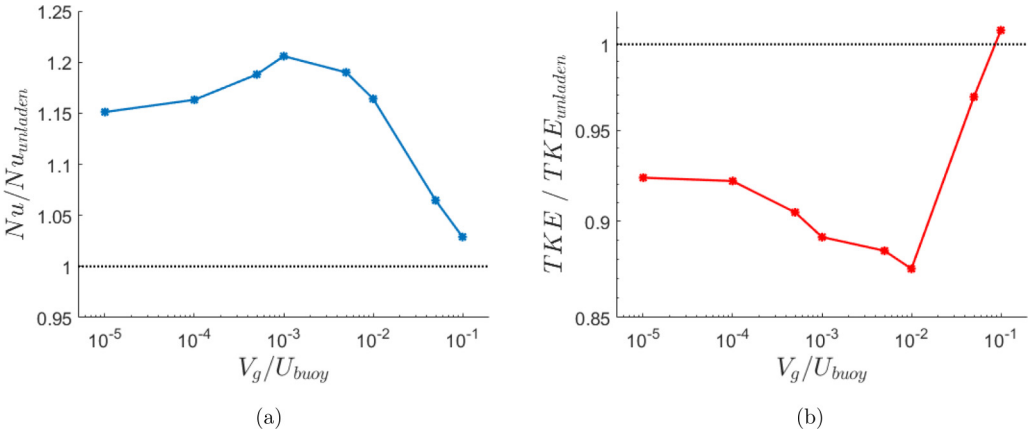

FIG. 5. Normalized (a) Nu and (b) TKE as a function of V_g/U_{buoy} for St ≈ 1 with two-way thermal and mechanical coupling. The dashed horizontal lines are the unladen values and reflect the unladen values.

Again, Nu is enhanced while TKE is suppressed for all St compared to the unladen values. Fig. 6(a) shows a distinct peak of Nu enhancement at St ≈ 1, which is associated with particle clustering [36,37]. In the limits of high and low St, Nu approaches its unladen value. The TKE of the system, however, has a more unique dependence on St, as shown in Fig. 6(b). Here there is not a single maximum of TKE reduction, and there exists a local minimum in TKE reduction at St ≈ 1. We note that for low St, Fig. 6(b) does not yet approach the unladen TKE as our thermal inertia based on τ_T is still non-negligible. Thus St ≈ 0.1 corresponds to St_T closer to 0.4, and we expect an approach to unladen values of TKE at even lower St. Given that we hold ϕ_m constant, these simulations are too expensive for the large number of small particles required.

In this flow particles have the ability to modify turbulence in two ways, via direct momentum coupling between phases, and through modifications to the temperature profile. To therefore better understand Fig. 6, Fig. 7 presents two of the normalized components of the heat flux: $\overline{q}_{\text{turb}} = \langle w'T' \rangle$, which is the turbulent heat flux, and $\overline{q}_{\text{part}}$, which is the vertical heat flux due to the particle source term S in Eq. (3). The modification of $\overline{q}_{\text{turb}}$ is nonmonotonic with St, in that maximum centerline reductions occur for both St ≈ 0.1 and St ≈ 2.5 (other St curves are not shown for clarity). These correspond to

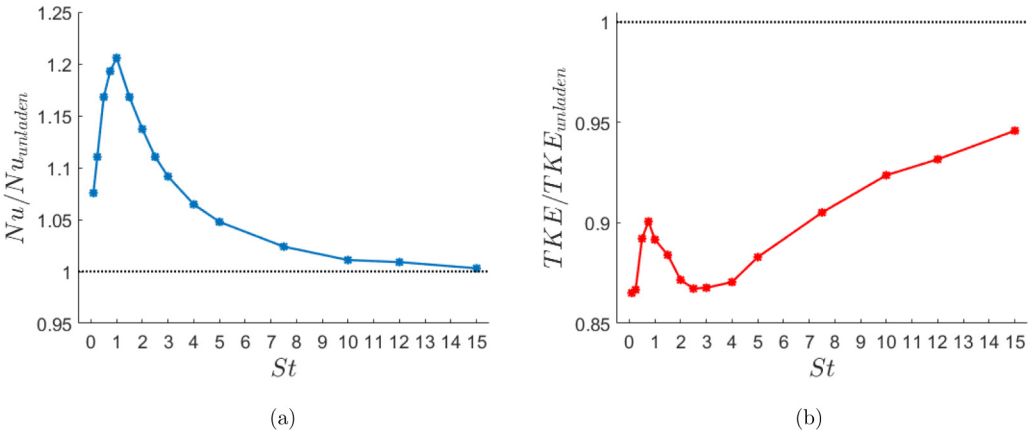

FIG. 6. Normalized (a) Nu and (b) TKE as a function of varying St for $V_g/U_{\text{buoy}} = 10^{-3}$ with two-way coupling. The horizontal lines are the unladen values.

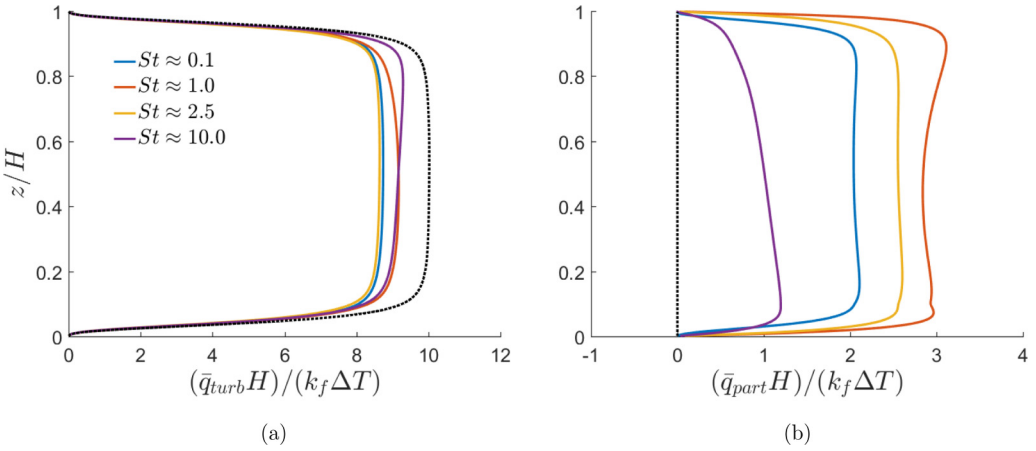

FIG. 7. Overall heat flux contributions due to (a) turbulent flux and (b) particle source flux.

the maximum TKE reductions in Fig. 6(b), which is consistent since buoyancy production of TKE is proportional to $\langle w'T' \rangle$. For these St, the primary effect of the particle is therefore to reduce buoyant production of TKE, while the effect of direct momentum coupling is much smaller (this is further discussed in the next section). The behavior of $\overline{q}_{\text{part}}$, meanwhile, exhibits only a single peak, with a maximum particle heat flux at St ≈ 1. This peak is associated with particles clustering in up- and downdrafts of the flow, and leads to the peak of Nu enhancement at St ≈ 1.

This additional mode of heat transfer, namely, that being carried by particles via $\overline{q}_{\text{part}}$, disrupts certain of the canonical features of Rayleigh-Bénard flow. For instance, the exact relationship between turbulence dissipation and heat transfer, $\epsilon = \nu^3 \text{Ra}(\text{Nu} - 1)/(H^4 \text{Pr}^2)$ [38], no longer holds because the two are not simply linked via local flow quantities. In the present case, for instance, dissipation ϵ is only slightly changed via two-way coupling [Fig. 8(a)], while Nu can be increased as a result of particles (Fig. 6).

Furthermore, in Fig. 8(b) it is found that, analogous to the turbulence dissipation ϵ, the thermal dissipation rate $\epsilon_T = \alpha_f \langle \nabla T' \cdot \nabla T' \rangle$, where $\nabla T'$ is the temperature fluctuation gradient, does not change significantly due to the particle thermal exchange with the fluid. The profiles in Fig. 8 suggest that dissipation (and other small-scale) mechanisms actually do remain intact in particle-laden

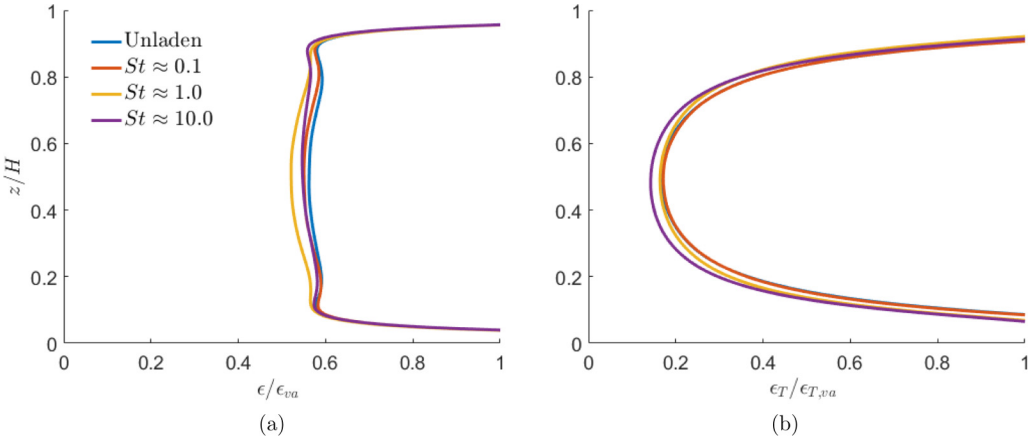

FIG. 8. Dissipation rate ϵ and thermal dissipation rate ϵ_T normalized by the vertical average (va) of its corresponding components. Plots have been zoomed in to highlight behavior in the domain center.

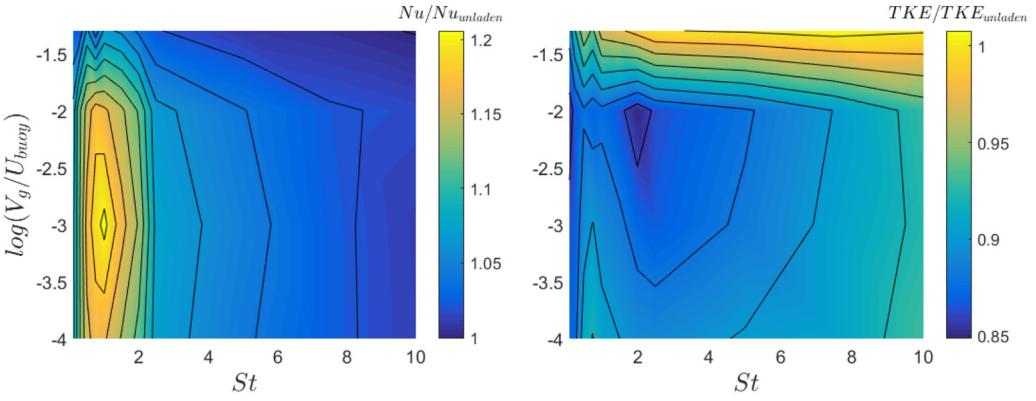

FIG. 9. Normalized (a) Nu and (b) TKE as a function of both St and $\log_{10}(V_g/U_{\text{buoy}})$. The solid lines represent evenly spaced contour levels for better clarity of the features.

Rayleigh-Bénard flow, and that the primary effect is the additional heat transfer mechanism through $\overline{q}_{\text{part}}$ and corresponding reduction of $\overline{q}_{\text{turb}}$.

Finally, as an overview of the behavior described above, Fig. 9 presents a two-dimensional contour map of the fractional change of Nu and TKE as a function of both St and V_g/U_{buoy}, compiled using over 30 simulations.

Several important features are noted. First, in Fig. 9(a), it is clear that the heat transfer enhancement due to particles is much more strongly affected by St than by settling velocity. The primary effect of V_g/U_{buoy} is to shut off the enhancement at sufficiently high values (returning to blue along the top of the figure). At all intermediate and low values of V_g/U_{buoy}, Nu behaves in the same way as shown in Fig. 6(a), a peak at St ≈ 1, falling off to the unladen value at asymptotically high or low values.

The turbulent kinetic energy, on the other hand, behaves in a more complex way as a function of St and V_g/U_{buoy}. First, for increasing inertia, the amount of gravitational settling needed to approach the unladen case decreases, as identified by the sloping boundary between yellow and blue at the upper right-hand corner of Fig. 9(b). Furthermore, the Stokes number corresponding to the minimum in TKE (i.e., the maximum reduction) also changes slightly with settling velocity, as seen by the orientation of the dark blue region on the left side of the contour map. This interdependence is related to the maximum centerline concentration seen in Fig. 2(b) at intermediate settling velocities, and Fig. 9(b) shows that the global minimum of TKE occurs for St ≈ 2 and $V_g/U_{\text{buoy}} \approx 10^{-2}$.

B. Coupling, specific heat ratio, and mass fraction

In the previous section we focused on the role of St and settling velocity on heat transfer and turbulence modulation, and we identified that St had the strongest effect on Nu and TKE. In this particle-laden Rayleigh-Bénard system, however, a few remaining factors can potentially influence the particle-turbulence interaction.

First, we consider the effects of coupling—thermal versus mechanical—by turning each on and off independently. We take St ≈ 1 and $V_g/U_{\text{buoy}} = 10^{-3}$ for all cases, and Fig. 10 shows the independent contributions of momentum and thermal coupling on both Nu and TKE. For any St, momentum coupling weakens the heat transfer, while thermal coupling enhances it. From Fig. 10(a), the thermal coupling overwhelms the momentum coupling effect, shown by the nearly identical Nu between the both and thermal coupling, resulting in an overall increase in Nu. Again, for limits of both high and low St, the unladen Nu is recovered. For St ≈ 1, the effect of preferential concentration exhibits itself only in the thermal coupling, whereas the changes in Nu due to momentum coupling only are a weak function of St.

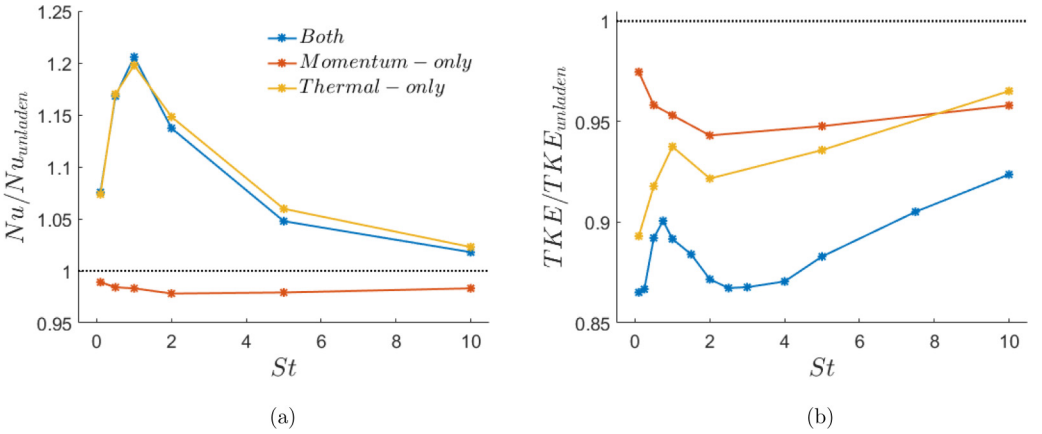

FIG. 10. Normalized (a) Nu and (b) TKE for all three types of couplings.

As previously discussed, the interplay between direct momentum coupling and thermally induced changes to buoyancy are both factors which vary the strength of TKE reduction. Figure 10(b) shows that, similar to Nu, the thermal coupling between phases is a larger portion of the overall effect of TKE. However in this case, the direct momentum coupling is similar in magnitude, and both work to reduce TKE compared to the unladen case. With only momentum coupling, a maximum attenuation is found at St ≈ 2, while thermal coupling again results in a local attenuation minimum around St ≈ 1. This local peak, seen in Fig. 6(b), is clearly a result of thermal coupling and as discussed above is caused by the thermally induced reduction of the turbulent heat flux $\overline{q}_{\text{turb}}$ [see Fig. 7(a)].

Second, all simulations presented in the previous section had a set specific heat ratio and mass fraction (see Table I). Again holding St ≈ 1 and $V_g/U_{\text{buoy}} = 10^{-3}$, we independently vary these quantities to assess their impact on Nu and TKE. Note that the thermal time scale, τ_T, will now vary with $C_{p,p}/C_{p,f}$, while the aerodynamic time constant, τ_p remains the same. This, in turn, will affect only St_T while the momentum-based St ≈ 1 is constant. Figure 11 shows the effect of changing the ratio $C_{p,p}/C_{p,f}$ over three orders of magnitude. Above and below a ratio $C_{p,p}/C_{p,f} \approx 1$, the behavior of Nu and TKE is distinct. For low $C_{p,p}/C_{p,f}$, the particles carry vanishingly small amounts of heat relative to the same mass of fluid and actually reduce Nu relative to the unladen case

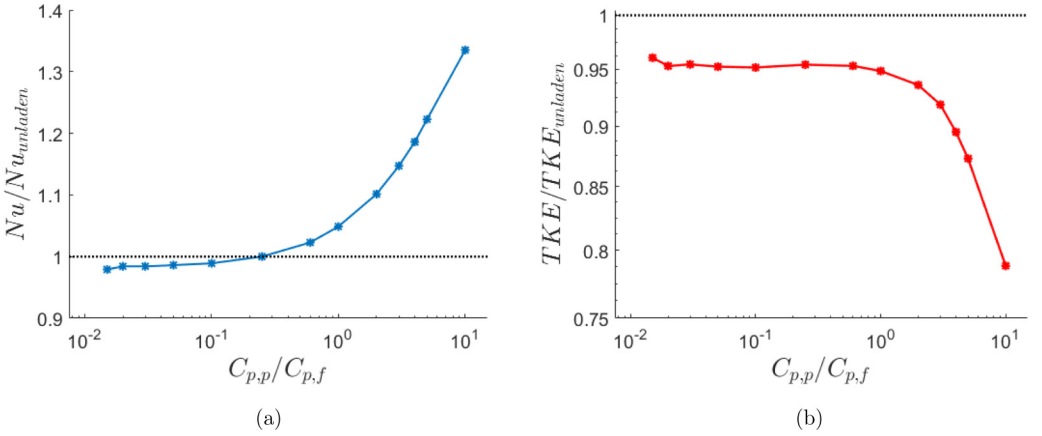

FIG. 11. Normalized (a) Nu and (b) TKE for varying $C_{p,p}/C_{p,f}$, holding St ≈ 1 and $V_g/U_{\text{buoy}} = 10^{-3}$ with both couplings.

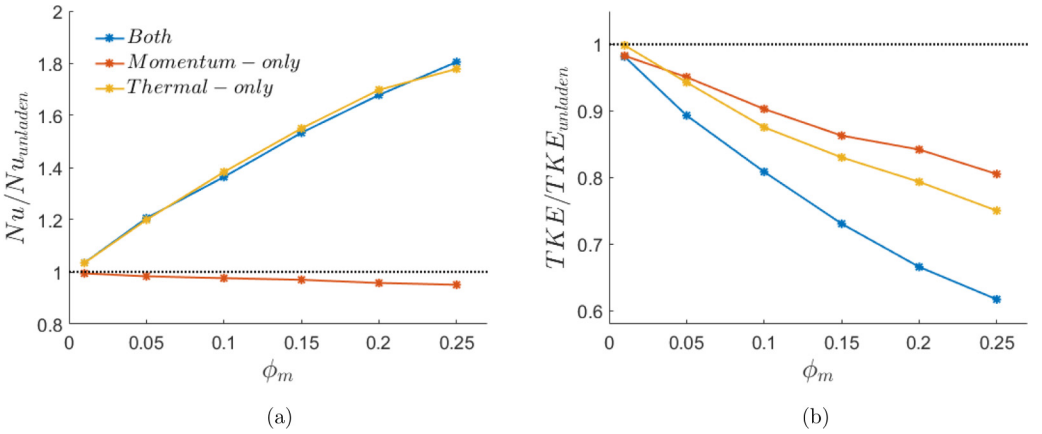

FIG. 12. Normalized (a) Nu and (b) TKE with all three types of couplings while varying ϕ_m at constant St ≈ 1 and $V_g/U_{\text{buoy}} = 10^{-3}$.

[Fig. 11(a)]. Since the carrying of heat by particles is one of the primary mechanisms for enhancing Nu [see Fig. 7(b)], reducing their heat capacity below that of the fluid means that the same mass of particles carries less heat than the same mass of fluid. Furthermore, in the limit of zero particle heat capacity, the flow is dominated by momentum coupling, which, as shown in Fig. 10(a), results in the attenuation of Nu. As $C_{p,p}/C_{p,f}$ increases above unity, the particles effectively become isothermal (a case considered by Oresta and Prosperetti [22]), and therefore Nu depends entirely on their initial temperature ($T_{p,\text{init}} = 305.15$ K, the average of the plate temperatures). For TKE [Fig. 11(b)] the results are similar: in the limit of small $C_{p,p}/C_{p,f}$, the attenuation of TKE saturates, since the flow is dominated by momentum coupling alone. As the heat capacity ratio increases, the enhanced thermal interaction between phases causes a larger decrease of buoyant TKE production, thereby reducing TKE relative to the unladen case.

Finally, Fig. 12 shows the influence of the mass fraction ϕ_m. In the limit of zero ϕ_m, the changes of Nu and TKE tend toward the unladen values as expected. From there, increased ϕ_m yields an enhancement of Nu (for both couplings) and an attenuation of TKE which is roughly linear with ϕ_m. For all combinations of thermal and mechanical coupling, this linear relationship is generally true, and for each ϕ_m, the relative balance between the different couplings is roughly the same. At higher values of ϕ_m, particle-particle interactions would require consideration [39].

IV. CONCLUSION

In this study, a DNS model is used to simulate canonical Rayleigh-Bénard flow laden with thermally and dynamically coupled particles, to investigate the response of turbulence and heat transfer. We focused in particular on the independent roles of particle inertia, as specified by the Stokes number, and the settling velocity, normalized by a buoyancy velocity scale, all at a constant Rayleigh number. In a broad sense, we are seeking an understanding of the nondimensional functionalities $\text{Nu}(\phi_m, C_{p,p}/C_{p,f}, \text{St}, V_g/U_{\text{buoy}})$ and $\text{TKE}(\phi_m, C_{p,p}/C_{p,f}, \text{St}, V_g/U_{\text{buoy}})$ at constant Ra. We find that the dependence of both of these quantities on the mass fraction ϕ_m is roughly proportional, and that both are relatively insensitive to V_g/U_{buoy} for $V_g/U_{\text{buoy}} < 10^{-2}$; above this, particles settle significantly towards the bottom of the domain, and the turbulence and heat transfer approach unladen values.

In this regime, the full dependence of Nu and TKE simplifies to $\text{Nu} = \phi_m f(\text{St}, C_{p,p}/C_{p,f})$ and $\text{TKE} = \phi_m g(\text{St}, C_{p,p}/C_{p,f})$, where f and g are dimensionless functions. At constant $C_{p,p}/C_{p,f}$, Nu and TKE ultimately become only a function of St, whose shape is indicated in Fig. 6. Likewise, in the limit of vanishing specific heat ratio ($C_{p,p}/C_{p,f} < 10^{-1}$), the particles become permanently

in thermal equilibrium with the flow, and the momentum coupling is the only means of particle influence on the flow; again St becomes the only meaningful independent parameter.

At all St, Nu was enhanced, while the effects of preferential concentration near St ≈ 1 resulted in a peak of Nu enhancement by up to 20%. Total integrated turbulent kinetic energy was found to be attenuated in all cases, due to both direct momentum coupling as well as reduced buoyancy production via particle-fluid thermal coupling. The primary cause of the enhancement of Nu is due to the direct particle contribution, as particles carry heat upwards during their vertical transport. The turbulent flux of heat is reduced, which is responsible for the decrease in TKE. The finding that thermal coupling overwhelms momentum coupling depends on the specific heat ratio, and in the limit of small $C_{p,p}/C_{p,f}$, momentum coupling dominates. In addition, we anticipate that momentum coupling may be more important relative to thermal coupling in the nondilute regime, where particle-particle collisions would need to be considered.

In this flow, where two-way coupling has multiple paths of influence (i.e., both thermal and mechanical coupling), we find a complex interplay between the direct momentum feedback between phases, and the modified buoyancy production of turbulent kinetic energy. As a result, some single-phase relationships (i.e., turbulence dissipation and heat transfer) that were established in previous studies are not applicable for coupled particles. Fruitful extensions of this system could include higher Rayleigh numbers, particle evaporation, or particle-particle interaction.

ACKNOWLEDGMENTS

This work was supported by the National Science Foundation (NSF) under Grant No. AGS-1429921 and the Office of Naval Research (ONR) under Grant No. N00014-16-1-2472. Computational resources were provided by the Notre Dame Center for Research Computing.

[1] A. W. Vreman, Turbulence attenuation in particle-laden flow in smooth and rough channels, J. Fluid Mech. **773**, 103 (2015).

[2] L. Zhao, H. I. Andersson, and J. J. J. Gillissen, Interphasial energy transfer and particle dissipation in particle-laden wall turbulence, J. Fluid Mech. **715**, 32 (2013).

[3] S. Sundaram and L. R. Collins, A numerical study of the modulation of isotropic turbulence by suspended particles, J. Fluid Mech. **379**, 105 (1999).

[4] M. Boivin, O. Simonin, and K. D. Squires, Direct numerical simulation of turbulence modulation by particles in isotropic turbulence, J. Fluid Mech. **375**, 235 (1998).

[5] J. Lee and C. Lee, Modification of particle-laden near-wall turbulence: Effect of Stokes number, Phys. Fluids **27**, 023303 (2015).

[6] J. Capecelatro and O. Desjardins, Mass loading effects on turbulence modulation by particle clustering in dilute and moderately dilute channel flows, J. Fluids Eng. **137**, 111102 (2015).

[7] D. H. Richter and P. P. Sullivan, Momentum transfer in a turbulent, particle-laden Couette flow, Phys. Fluids **25**, 053304 (2013).

[8] F. Zonta, C. Marchioli, and A. Soldati, Direct numerical simulation of turbulent heat transfer modulation in micro-dispersed channel flow, Acta Mech. **195**, 305 (2008).

[9] B. Shotorban, F. Mashayek, and R. V. R. Pandya, Temperature statistics in particle-laden turbulent homogeneous shear flow, Int. J. Multiphase Flow **29**, 1333 (2003).

[10] J. G. M. Kuerten, C. W. M. van der Geld, and B. J. Geurts, Turbulence modification and heat transfer enhancement by inertial particles in turbulent channel flow, Phys. Fluids **23**, 123301 (2011).

[11] M. H. Nakhaei and B. Lessani, Effects of solid inertial particles on the velocity and temperature statistics of wall bounded turbulent flow, Int. J. Heat Mass Transf. **106**, 1014 (2017).

[12] D. H. Richter and P. P. Sullivan, Modification of near-wall coherent structures by inertial particles, Phys. Fluids **26**, 103304 (2014).

[13] C. D. Dritselis and N. S. Vlachos, Numerical investigation of momentum exchange between particles and coherent structures in low Re turbulent channel flow, Phys. Fluids **23**, 025103 (2011).

[14] M. Righetti and G. P. Romano, Particle-fluid interactions in a plane near-wall turbulent flow, J. Fluid Mech. **505**, 93 (2004).
[15] D. H. Richter, Turbulence modification by inertial particles and its influence on the spectral energy budget in planar Couette flow, Phys. Fluids **27**, 063304 (2015).
[16] A. Frankel, H. Pouransari, F. Coletti, and A. Mani, Settling of heated particles in homogeneous turbulence, J. Fluid Mech. **792**, 869 (2016).
[17] R. Zamansky, F. Coletti, M. Massot, and A. Mani, Radiation induces turbulence in particle-laden fluids, Phys. Fluids **26**, 071701 (2014).
[18] R Zamansky, F Coletti, M Massot, and A Mani, Turbulent thermal convection driven by heated inertial particles, J. Fluid Mech. **809**, 390 (2016).
[19] R. Lakkaraju, L. E. Schmidt, P. Oresta, F. Toschi, R. Verzicco, D. Lohse, and A. Prosperetti, Effect of vapor bubbles on velocity fluctuations and dissipation rates in bubbly Rayleigh-Bénard convection, Phys. Rev. E **84**, 036312 (2011).
[20] P. Oresta, R. Verzicco, D. Lohse, and A. Prosperetti, Heat transfer mechanisms in bubbly Rayleigh-Bénard convection, Phys. Rev. E **80**, 026304 (2009).
[21] R. Lakkaraju, R. J. A. M Stevens, P. Oresta, R. Verzicco, D. Lohse, and A. Prosperetti, Heat transport in bubbling turbulent convection, Proc. Natl. Acad. Sci. USA **110**, 9237 (2013).
[22] P. Oresta and A. Prosperetti, Effects of particle settling on Rayleigh-Bénard convection, Phys. Rev. E **87**, 063014 (2013).
[23] M. R. Maxey and J. J. Riley, Equation of motion for a small rigid sphere in nonuniform flow, Phys. Fluids **26**, 883 (1983).
[24] W. E. Ranz and W. R. Marshall, Evaporation from drops, Chem. Eng. Prog. **48**, 141 (1952).
[25] D. H. Richter and P. P. Sullivan, The sea spray contribution to sensible heat flux, J. Atmos. Sci. **71**, 640 (2014).
[26] D. H. Richter, O. Garcia, and C. Astephen, Particle stresses in dilute, polydisperse, two-way coupled turbulent flows, Phys. Rev. E **93**, 013111 (2016).
[27] B. Helgans and D. H. Richter, Turbulent latent and sensible heat flux in the presence of evaporative droplets, Int. J. Multiphase Flow **78**, 1 (2016).
[28] J. F. Kok, E. J. R. Parteli, T. I. Michaels, and D. Bou Karam, The physics of wind-blown sand and dust, Rep. Prog. Phys. **75**, 106901 (2012).
[29] E. Radziemska and W. M. Lewandowski, Heat transfer by natural convection from an isothermal downward-facing round plate in unlimited space, Appl. Energy **68**, 347 (2001).
[30] K. D. Squires and J. K. Eaton, Particle response and turbulence modification in isotropic turbulence, Phys. Fluids A **2**, 1191 (1990).
[31] A. Aliseda, A. Cartellier, F. Hainaux, and J. C. Lasheras, Effect of nonlinear drag on the settling velocity of particles in homogeneous isotropic turbulence, J. Fluid Mech. **468**, 77 (2002).
[32] L.-P. Wang and M. R. Maxey, Settling velocity and concentration distribution of heavy particles in homogeneous isotropic turbulence, J. Fluid Mech. **256**, 27 (1993).
[33] G. Sardina, P. Schlatter, L. Brandt, F. Picano, and C. M. Casciola, Wall accumulation and spatial localization in particle-laden wall flows, J. Fluid Mech. **699**, 50 (2012).
[34] C. Marchioli and A. Soldati, Mechanisms for particle transfer and segregation in a turbulent boundary layer, J. Fluid Mech. **468**, 283 (2002).
[35] R. Monchaux, M. Bourgoin, and A. Cartellier, Preferential concentration of heavy particles: A Voronoï analysis, Phys. Fluids **22**, 103304 (2010).
[36] K. D. Squires and J. K. Eaton, Measurements of particle dispersion obtained from direct numerical simulations of isotropic turbulence, J. Fluid Mech. **226**, 1 (1991).
[37] D. W. I. Rouson and J. K. Eaton, On the preferential concentration of solid particles in turbulent channel flow, J. Fluid Mech. **428**, 149 (2001).
[38] G. Ahlers, S. Grossmann, and D. Lohse, Heat transfer and large scale dynamics in turbulent Rayleigh-Bénard convection, Rev. Mod. Phys. **81**, 503 (2009).
[39] S. Balachandar and J. K. Eaton, Turbulent dispersed multiphase flow, Annu. Rev. Fluid Mech. **42**, 111 (2010).